1 Vector Magnetic Field Synoptic Charts from the
2 *Helioseismic and Magnetic Imager* (HMI)

3 **Yang Liu**[1] · **J. Todd Hoeksema**[1] · **Xudong**
4 **Sun**[1] · **Keiji Hayashi**[2] ·

6 **Abstract**
7 Vector magnetic field synoptic charts from the *Helioseismic and Magnetic*
8 *Imager* (HMI) are now available for each Carrington Rotation (CR) starting
9 from CR 2097 in May 2010. Synoptic charts are produced using 720-second
10 cadence full-disk vector magnetograms remapped to Carrington coordinates.
11 The vector field is derived from the Stokes parameters (I, Q, U, V) using a Milne-
12 Eddington based inversion model. The 180° azimuth ambiguity is resolved using
13 the Minimum Energy algorithm for pixels in active regions and for strong-field
14 pixels (the field is greater than about 150 G) in quiet Sun regions. Three other
15 methods are used for the rest of the pixels: the potential-field method, the radial-
16 acute angle method, and the random method. The vector field synoptic charts
17 computed using these three disambiguation methods are evaluated. The noise
18 in the three components of vector magnetic field is generally much higher in the
19 potential-field method charts. The component noise levels are significantly differ-
20 ent in the radial-acute charts. However, the noise levels in the random-method
21 charts are lower and comparable. The assumptions used in the potential-field
22 and radial-acute methods to disambiguate the weak transverse field introduce
23 bias that propagates differently into the three vector-field components, leading to
24 unreasonable pattern and artifacts, whereas the random method appears not to
25 introduce any systematic bias. The computed current sheet on the source surface,
26 computed using the potential-field source-surface model applied to random-
27 method charts, agrees with the best solution (the result computed from the
28 synoptic charts with the minimum energy algorithm applied to each and every
29 pixel in the vector magnetograms) much better than the other two. Differences in
30 the synoptic charts determined with the best method and the random method
31 are much smaller than those from the best method and the other two. This
32 comparison indicates that the random method is better for vector field synoptic
33 maps computed from near-central meridian data. Thus, the vector field synoptic
34 charts provided by the *Joint Science Operations Center* (JSOC) are produced
35 with the random method.

36 **Keywords:** Magnetic fields, photosphere · HMI: vector magnetic field · Synoptic
37 chart

[1] W. W. Hansen Experimental Physics Laboratory, Stanford
University, Stanford, CA94305-4085, USA email:
yliu@sun.stanford.edu
[2] Institute for Space-Earth Environmental Research, Nagoya
University, Nagoya Aichi 464-8601, Japan

1. Introduction

The HMI (Scherrer *et al.*, 2012; Schou *et al.*, 2012) vector magnetic fields synoptic charts for each Carrington rotation for the entire *Solar Dynamics Observatory* (SDO) (Pesnell *et al.*, 2012) mission are available now through the JSOC. They are computed from 720-second cadence full-disk vector magnetograms (Hoeksema *et al.*, 2014). The data series names are hmi.B_synoptic for full-resolution synoptic charts of 3600×1440 and hmi.B_synoptic_small for a smaller size of 720×360. The x-axis corresponds to longitude in degrees and the y-axis to equal steps in sine latitude. In this report, we describe the procedure for producing synoptic charts from HMI magnetograms and evaluate the disambiguation method chosen to resolve the $180°$ ambiguity of the azimuth in vector magnetic field measurement.

The report is organized as follows: Section 2 describes the input data and the procedure for producing synoptic maps. Vector field synoptic charts produced using data with different disambiguation methods are described in Section 3. A quantitative comparison of the different maps is given in Section 4. We summarize the results in Section 5.

2. Data and Methods

2.1. Full-disk Vector Magnetic Field Data

The vector magnetic field synoptic charts reported here are produced from the HMI full-disk vector magnetograms (Hoeksema *et al.*, 2014). The HMI instrument is a filtergraph covering the full solar disk with 4096×4096 pixels. The spatial resolution is about 1" with a 0.5" pixel size. The width of the filter profiles is $76 \, \text{mÅ}$. The spectral line used is Fe I 6173 Å, which forms in the photosphere (Norton *et al.*, 2006). There are two CCD cameras in the instrument: the front camera and the side camera. Until 13 April 2016 only data from the side camera were used to measure the vector magnetic field and the frame list took 135 seconds to obtain the necessary filtergrams in six polarization states at six wavelength positions. The front camera measures the circular polarizations only. Since 13 April 2016, filtergrams from both cameras are combined and the basic vector-field sequence completes in 90 seconds. The Stokes parameters (I, Q, U, V) are computed from those measurements (Couvidat *et al.*, 2016), and are further inverted to retrieve the vector magnetic field using a Milne-Eddington (ME) based inversion algorithm, Very Fast Inversion of the Stokes Vector (VFISV; Borrero *et al.*, 2011; Centeno *et al.*, 2014). To suppress p modes and to increase the signal-to-noise ratio, the registered filtergrams are usually averaged over a certain time before computing the Stokes vector. Currently a weighted average is computed every 720 seconds using data obtained over 1350 seconds.

Inversion of the vector field has an unavoidable $180°$ ambiguity in the azimuthal field direction. Assumptions about the field must be made to resolve the ambiguity. For all pixels in active regions, as well as for strong-field pixels (where the field strength is greater than about 150 G) in quiet Sun regions, the azimuth

is determined using a minimum energy algorithm (Metcalf, 1994; Metcalf *et al.*, 2006; Leka *et al.*, 2009). The minimum-energy-method computation is time consuming in pixels where the signal is dominated by noise, so for weaker field regions in the quiet Sun (most of the disk, where the total field strength is below about 150 G) we resolve the 180° ambiguity using three simpler and quicker methods: the potential-field method (potential method hereafter), the radial acute-angle method (radial method), and the random method.

The potential method resolves the 180° ambiguity in such a way that the observed and potential transverse field components form an acute angle. The potential field is computed from the well-observed line-of-sight field using a fast Fourier transform method. In this computation, the solar disk is divided into 900 rectangular tiles in a Mollweide equal area projection, where the potential field is calculated assuming a local Cartesian geometry. The radial method chooses the direction of the transverse field such that the field vector is closer to the local radial direction. The random method assumes that there is not enough information to disambiguate the azimuth and so randomly assigns the disambiguation direction of the transverse field for each pixel. All three solutions are saved in the HMI full-disk vector magnetic field data series. More details on how the HMI vector magnetograms are processed can be found in Hoeksema *et al.* (2014).

2.2. Method for Producing Synoptic Charts

Synoptic maps constructed from HMI full-disk vector magnetograms are now available for the entire SDO mission, starting 1 May 2010. The first step is to transform the components of the HMI 720-second vector magnetograms from field strength, inclination, azimuth, and disambiguation into three field components in heliographic coordinates: B_r, B_θ and B_ϕ. This is done for all vector magnetograms of good quality as determined by the keyword QUALITY[1]. The keyword QUALITY contains information about possible issues in the collection and processing of each magnetogram. More information can be found in http://jsoc.stanford.edu/doc/data/hmi/Quality_Bits/QUALITY.txt.

Second, each of the three components undergoes a spatial cubic interpolation onto a regular, evenly spaced Carrington grid in longitude and sine latitude. The Carrington coordinate for each observed point is adjusted to account for differential rotation relative to the time of central meridian crossing; this minimizes smearing when multiple observations are averaged, as suggested by Ulrich *et al.* (2002). The remapping is done in two steps. Initially the remapped grid is interpolated to the spatial resolution of the disk-center pixel, i.e., 0.033°. Then the resolution is reduced to 0.1° using a nine-pixel box-car average. This results in a rectangular longitude– sine-latitude map for each component with nominal dimensions 1800 × 1440. Magnetogram data out to 0.998 solar radii are used. Limb pixels and seasonally unobserved parts of the map near the poles are missing.

The remapped, resized vector magnetograms are then combined to produce synoptic charts. The vector data measured at each Carrington coordinate in the

---

[1]The QUALITY filter used here is 0xfffefb00.

final map averages data from exactly twenty contributing magnetograms. The average is computed using measurements from the 20 720-second magnetograms that contribute pixels observed closest to central meridian. Outliers are excluded from the average if the value departs from the median by more than three times the rms. If a measurement is excluded, the value from another magnetogram observed next-closest to central meridian is added. We find that one outlier is identified in about 20% of the synoptic pixels; about 1.6% of the synoptic pixels have two or more outliers. The effective temporal width of the HMI synoptic-map contribution is about 4 hours at each Carrington longitude, i.e., data are observed within 2 hours of central meridian passage. This means that the contributing pixels are observed within about $\pm 1.2°$ of central meridian. The final synoptic charts have a size of 3600 × 1440, with the x-axis referring to longitude in degrees, and the y-axis to equal steps in sine latitude. At the equator observations from approximately 180 magnetogram pixels contribute to each value in the synoptic chart. JSOC also provides vector field synoptic charts with a smaller size of 720 × 360. These smaller maps are produced from the regular size maps using a box car average. The following analysis is based on the regular size maps (3600 × 1440).

We note that the same basic procedure is applied to create the standard HMI synoptic maps that are based on line-of-sight (LoS) magnetograms, e.g. synoptic data series hmi.Synoptic_Mr_720s. The primary difference is that the first step is to infer a radial field from the line-of-sight magnetogram measurement by dividing the observed value by the cosine of the distance from disk center. Liu *et al.* (2012) describe the HMI line-of-sight magnetograms and compare magnetic field results from HMI and the Michelson Doppler Imager (MDI). The alternative synoptic charts that report the line-of-sight component of the field based on LoS magnetograms, are derived from the radial synoptic maps by multiplying by cosine latitude. The series of this data product is hmi.Synoptic_Ml_720s. The HMI convention is to use 'M' in the series name for magnetic field products that come from LoS magnetograms and 'B' for magnetic field products based on vector magnetograms.

3. HMI Vector Field Synoptic Charts: 180° Disambiguation with Different Methods

Assumptions that are used to disambiguate the weak transverse field may introduce bias, which propagates differently into the B_r, B_θ, and B_ϕ components, leading to unreasonable patterns and artifacts. This needs to be evaluated in order to choose a better disambiguation method for vector-field synoptic charts. In this section, we describe vector field synoptic charts computed with azimuths based on the three disambiguation methods. A more quantitative analysis is presented in the next section.

Figure 1 shows synoptic charts of B_r (top), B_ϕ (middle), and B_θ (bottom) for CR 2145 that was observed at central meridian from December 18, 2013 to January 16, 2014. Disambiguation in quiet-Sun regions is done using the potential method. All the images shown here saturate at ± 80.0 G. The figure
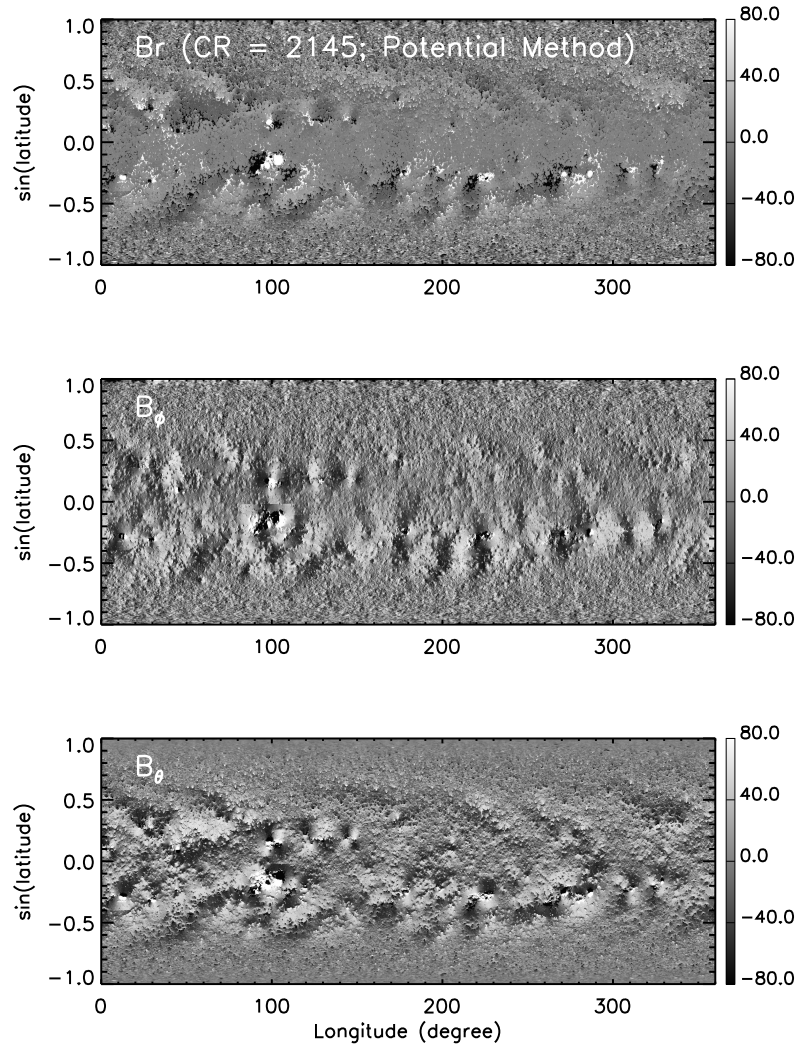
Figure 1. Vector magnetic field synoptic chart for Carrington Rotation 2145 from 18 December 2013 to 16 January 2014. From top to bottom the panels show B_r, B_ϕ, and B_θ. The 180° degree ambiguity of the azimuth is resolved using the minimum energy algorithm for strong field pixels (where the field is greater than about 150 G), and the potential method for weak-field pixels in quiet Sun regions. See text for details.

shows obvious large-scale shadow-like patterns surrounding stronger magnetic field patches in all three field components. This cannot be real.

In the B_r map (top panel), positive field patches have positive-field shadows toward higher latitude and negative-field shadows toward lower latitude. The shadows for negative-field patches are the opposite: negative-field shadows are toward higher latitude and positive-field shadows toward lower latitude. The shadows are a natural consequence of the potential method. The model potential field used in the disambiguation must diverge from positive patches and

175 converge toward negative patches. The direction of the transverse component of
176 the potential field always points from regions of positive field toward negative. At
177 most pixels in quiet-Sun regions the total field strength is less than the noise level
178 in the transverse field component. In the original magnetogram, the quiet-Sun
179 noise level in the transverse-field measurement is about 100 G, about ten times
180 higher than the line-of-sight component. The noise level varies with position
181 and time (Hoeksema *et al.*, 2014). Thus B_r in quiet-Sun regions is determined
182 mostly by the systematic pattern in the transverse field that points from positive
183 to negative field regions. This causes the shadow-like patterns in B_r, as well as
184 the large-scale shadow-like patterns in B_θ and B_ϕ maps. The figure confirms
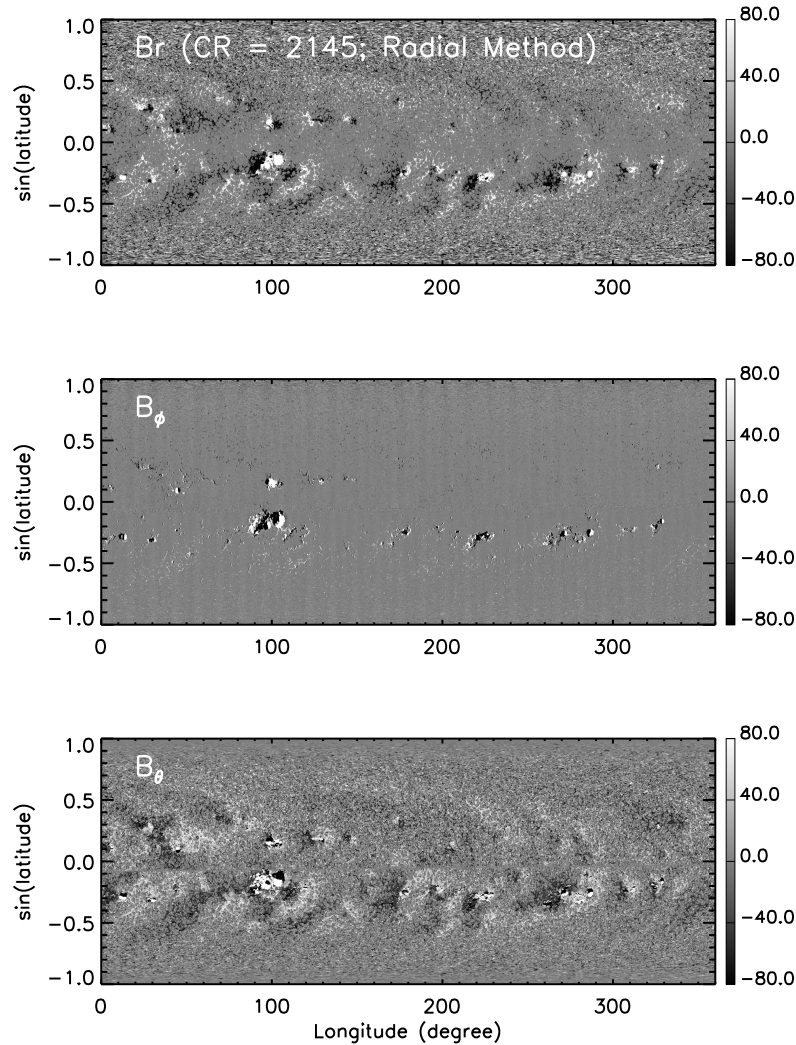185 that the potential method introduces artificial patterns in the synoptic map.

Figure 2. Same as Figure 1, but the 180° degree ambiguity of the azimuth is resolved using the radial method for the weak-field pixels.

Figure 2 shows the charts for the same Carrington Rotation with disambigua-
tion determined using the radial method. This figure reveals another systematic
error – there is significantly different noise in the B_θ and B_ϕ components. This
arises because of a geometrical bias in the way the noisier transverse component
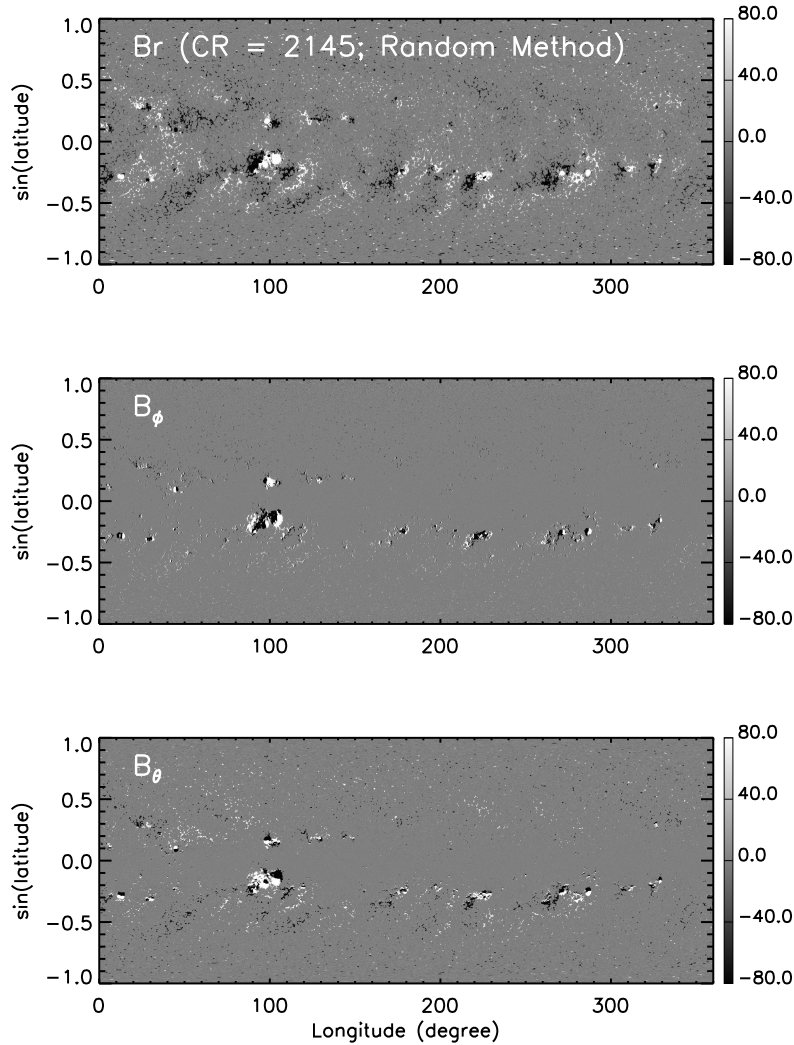of the field affects the disambiguation.

Figure 3. Same as in Figure 1, but the $180°$ degree ambiguity of the azimuth is resolved
using the random method for the weak-field pixels.

The B_r map (top panel) has low background noise near the equator, but be-
comes much noisier with increasing latitude. This is due to the noisier transverse
field that is dominant in quiet-Sun regions. The contribution of the transverse
field component to B_r increases toward the poles.

B_ϕ map (middle panel) looks suspiciously clean everywhere. Because the data
used to produce the synoptic chart are measured very close to central meridian,

197 the east-west component of the transverse field is approximately equal to B_ϕ,
198 and B_ϕ depends very little on the radial field component. Therefore the azimuth
199 direction of B_ϕ chosen with the radial method is fairly random. This means
200 that B_ϕ in quiet-Sun regions is determined mainly by the well-measured line-of-
201 sight field component only, whereas the essentially random contributions from
202 the transverse-field component cancels out after averaging. Contributions from
203 line-of-sight field generate the small-scale magnetic features seen in the B_ϕ maps
204 in the quiet-Sun regions. It is also interesting to note that B_ϕ becomes much
205 noisier near the equator (see plot in next section). This equatorial noise increase
206 happens because the line-of-sight field is very close to radial and it contributes
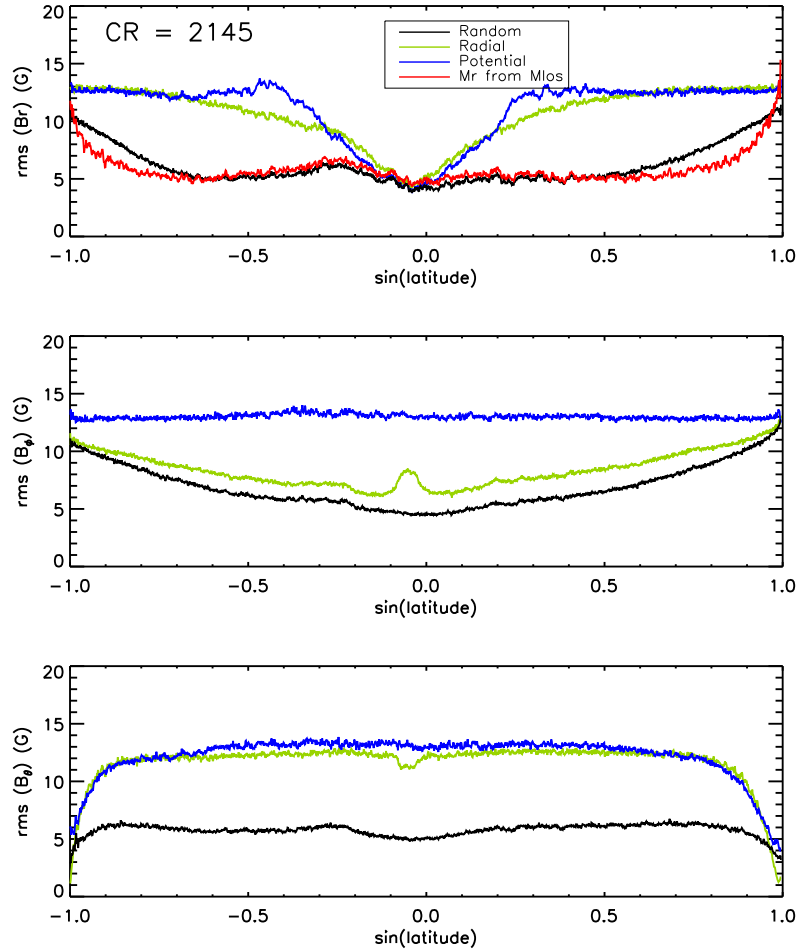207 very little to B_ϕ.

Figure 4. Quantitative comparison of quiet-Sun noise levels in synoptic charts. The rms in B_r (top), B_ϕ (middle), and B_θ (bottom) as a function of sine latitude for CR 2145. The curves with different colors refer to synoptic charts produced with different disambiguation methods, as marked in the legend in the top panel. For reference the rms of the inferred radial field component, M_r, computed from the standard synoptic chart produced using HMI line-of-sight magnetograms is also presented in the top panel (red curve).

208   In contrast, the B_θ map (bottom panel of Figure 2) shows a great deal of
209 structure. The structures are an artifact of the radial method of disambiguation.
210 The radial method determines the disambiguated direction of the transverse
211 field in each pixel such that its projection to the radial direction must have
212 the same sign as that of the line-of-sight field. Any photospheric patch having
213 coherent structure in the line-of-sight field (e.g. remnant active region patches
214 at high latitudes with a particular sign), will impose a preferred direction in
215 the transverse field. This well-organized transverse field enhances patterns in
216 B_θ maps that are originally present in the line-of-sight field. Similar to B_ϕ, B_θ
217 appears to be purely noise near the equator.

218   The most obvious problem in the radial-method synoptic maps is the signifi-
219 cant difference in noise in the field components: the noise differs substantially in
220 B_θ and B_ϕ maps. This is certainly not real. Such a systematic bias has potential
221 to jeopardize utility of the maps, such as for numerical simulations.

222   The random method appears to produce maps without artificial patterns
223 and the noise in the three components is comparable (see Figure 3). A possible
224 disadvantage of the random method is that, if there is any information in the
225 transverse field components in the quiet-Sun, then this method does not take
226 advantage of it.

4. Quantitative Comparison of Vector-Field Synoptic Charts

228 Figure 4 gives a quantitative comparison of the root-mean-square (rms) for B_r
229 (top), B_ϕ (middle), and B_θ (bottom) as a function of sine latitude for the three
230 types of synoptic charts. The top panel also shows the rms of the inferred radial
231 field (M_r, in red) from the standard synoptic map constructed using HMI line-
232 of-sight magnetograms. The rms for each latitude is computed from pixels at all
233 longitudes (up to 3600 pixels in total) that have a field strength less than 23
234 G, about 3 times the standard deviation of the field. As expected, the noise in
235 the three components is generally much higher in the potential-method charts,
236 and significantly different in the radial-method charts. The noise in the random-
237 method charts is lower and is comparable for all three components. The noise in
238 B_r is also consistent with the rms of M_r in the standard synoptic map (red curve
239 in the top panel). This suggests that, among the three methods, the random
240 method produces the lowest noise at all latitudes.

241   To further assess the impact of the various weak-field disambiguation meth-
242 ods, we also processed the HMI vector field data for CR 2145 by applying the
243 minimum energy disambiguation method (annealing method hereafter) to each
244 and every pixel. The photospheric vector field determined in this way can be
245 considered to have the best disambiguation, and can therefore be used to assess
246 results from other maps.

247   Shown in Figure 5 are differences of B_r (top), B_ϕ (middle), and B_θ (bot-
248 tom) between the potential-method maps and the annealing-method maps for
249 CR 2145. Here $\delta B_r = B_r(\text{potential-method}) - B_r(\text{annealing-method})$, $\delta B_\phi =$
250 $B_\phi(\text{potential-method}) - B_\phi(\text{annealing-method})$, and $\delta B_\theta = B_\theta(\text{potential-method}) - B_\theta(\text{annealing-}$
251 method). All three difference images show obvious patterns, indicating that

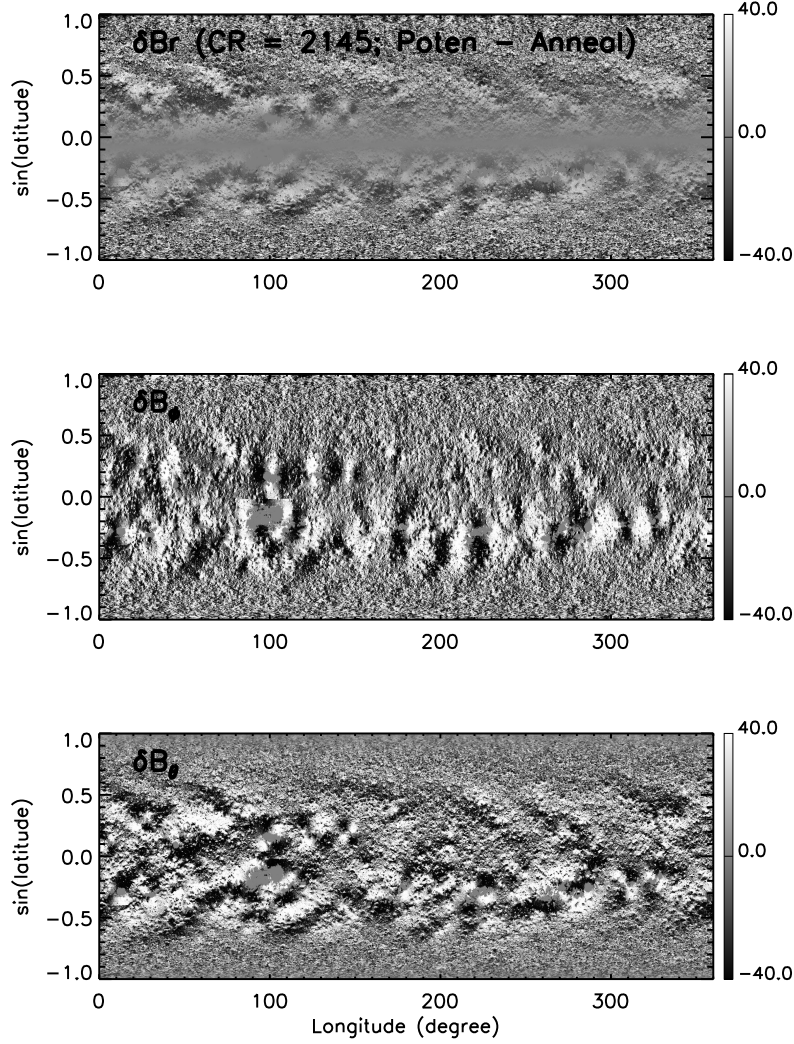**Figure 5.** Difference images of B_r (top), B_ϕ (middle), and B_θ (bottom) between the potential-method synoptic chart and the annealing-method chart for CR 2145. Top: $\delta B_r = B_r(\text{potential-method}) - B_r(\text{annealing-method})$; Middle: $\delta B_\phi = B_\phi(\text{potential-method}) - B_\phi(\text{annealing-method})$; Bottom: $\delta B_\theta = B_\theta(\text{potential-method}) - B_\theta(\text{annealing-method})$. All three images are scaled at ± 40 G. Medians of $|\delta B_r|$, $|\delta B_\phi|$, and $|\delta B_\theta|$ are 9.6 G, 24.4 G, and 18.2 G, respectively.

the potential-method produces artificial structures. This is consistent with the results in the previous Section.

Figure 6 shows difference images between the radial-method and the annealing-method synoptic charts. δB_r (top) increases with latitude, and large-scale patterns are also visible at low latitude. While δB_ϕ (middle) is fairly small and smooth, δB_θ (bottom) has obvious structures. This confirms that the radial-
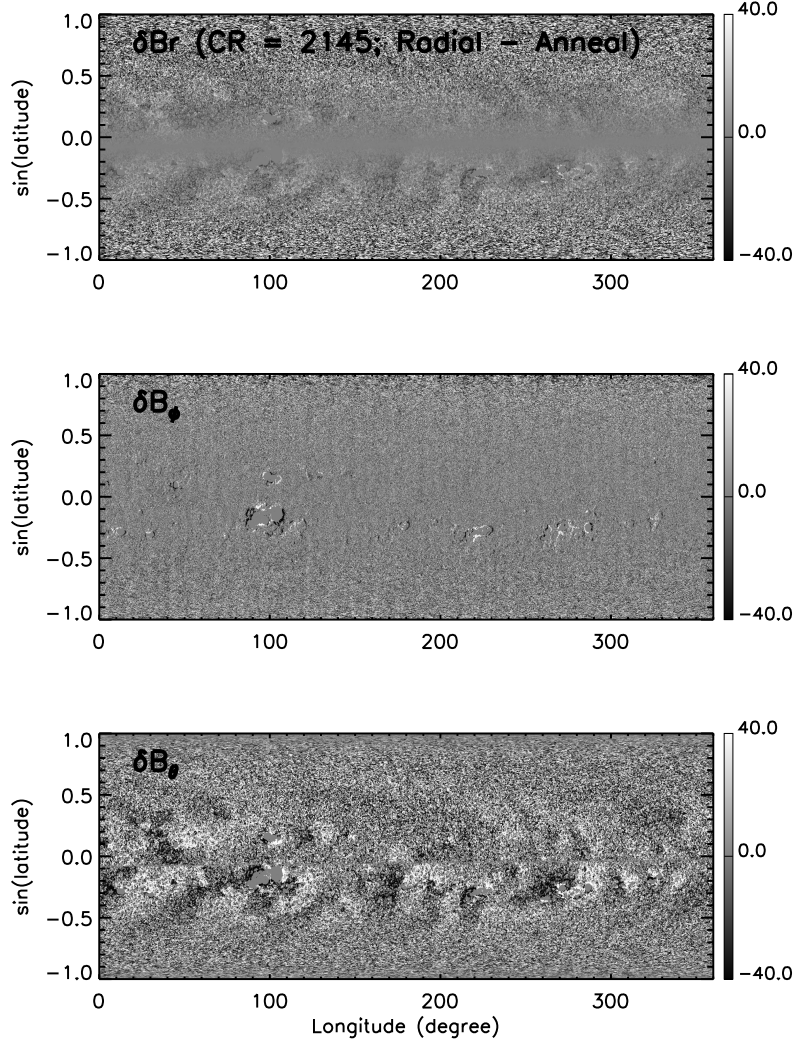
Figure 6. Same as Figure 5, but the difference images between the radial-method synoptic chart and the annealing-method chart. Medians of $|\delta B_r|$, $|\delta B_\phi|$, and $|\delta B_\theta|$ are 8.2 G, 10.2 G, and 15.5 G, respectively.

258 method not only produces artificial structures in B_θ maps, but also causes
259 significantly different noises in B_ϕ and B_θ maps.
260   No systematic patterns are visible in difference images of B_r, B_ϕ, and B_θ
261 between the random-method and the annealing-method charts (see Figure 7).
262 Only δB_r becomes slightly large at the high latitude.
263   More quantitatively, we calculate median of the differences from the data
264 shown in Figures 5–7. The median value for each latitude is computed from
265 pixels at all longitudes. Figure 8 shows medians of $|\delta B_r|$ (top), $|\delta B_\phi|$ (middle),
266 and $|\delta B_\theta|$ (bottom) as a function of sine latitude. For reference, we also plot
267 the median of $|M_r - B_r|$ (red curve in the top panel), where B_r is from the
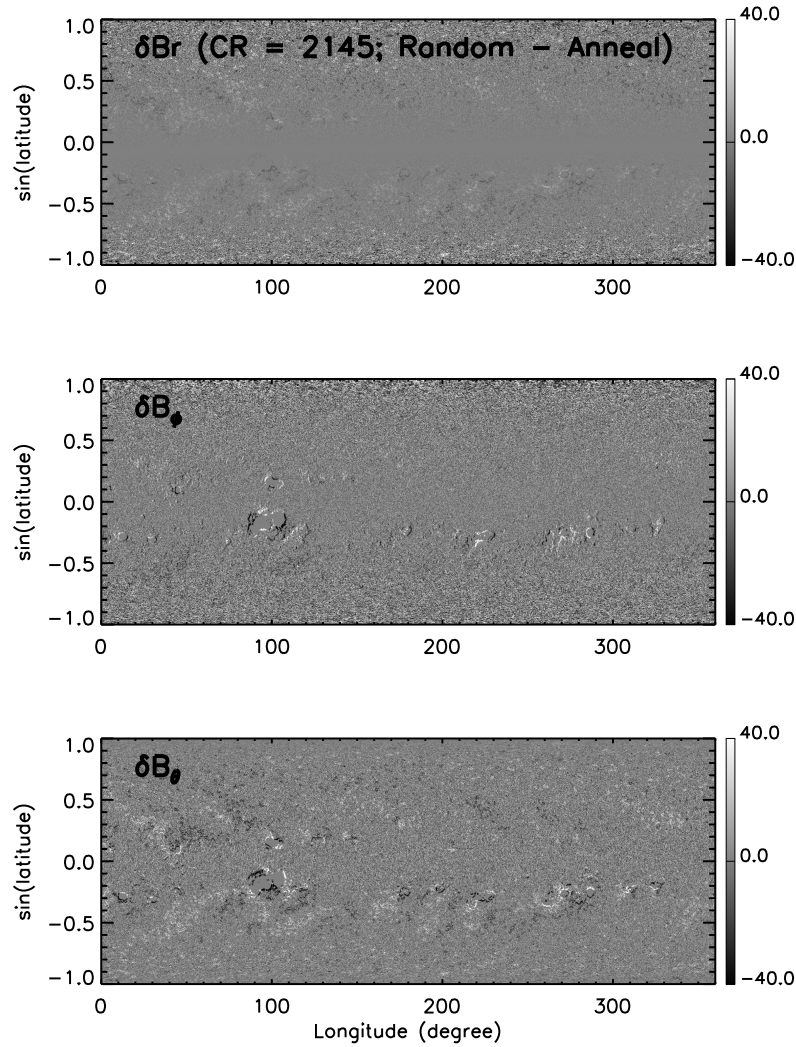
Figure 7. Same as Figure 5, but the difference images are between the random-method synoptic chart and the annealing-method chart. Medians of $|\delta B_r|$, $|\delta B_\phi|$, and $|\delta B_\theta|$ are 3.9 G, 9.6 G, and 7.4 G, respectively.

268 annealing-method, and the M_r from the HMI line-of-sight magnetograms. This
269 plot gives a quantitative measure of the differences, and thus can be used to
270 assess the goodness of the disambiguation methods. The random-method gives
271 smaller medians in all three components and at all latitudes than the other two.
272 This suggests the random method is the best of the three methods for synoptic
273 maps. Median of the random-method $|\delta B_r|$ is also very close to that of the
274 $|\delta M_r| = |M_r - B_r|$, except near the polar region where the median of $|\delta M_r|$
275 becomes very large. It is due to the method used to convert the line-of-sight
276 field to the radial field: the line-of-sight field is divided by cosine center-to-limb
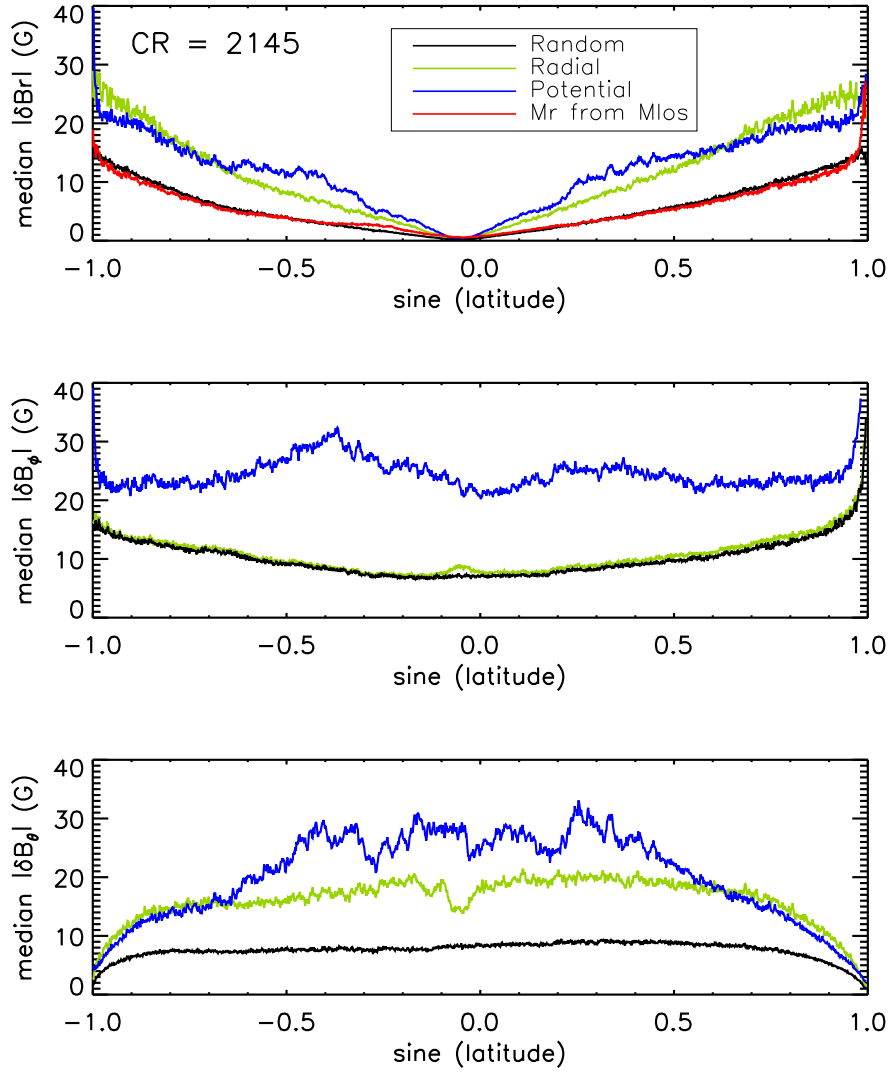277 angle that is very small near the pole.

Figure 8. Quantitative comparison of the differences between the annealing-method synoptic chart and the synoptic charts from the three other methods. The medians of $|\delta B_r|$ (top), $|\delta B_\phi|$ (middle), and $|\delta B_\theta|$ (bottom) are plotted as a function of sine latitude for CR 2145. The curves with different colors refer to synoptic charts produced with different disambiguation methods, as marked in the legend in the top panel. For reference the median of difference between the inferred radial field component, M_r, computed from the standard synoptic chart produced using HMI line-of-sight magnetograms, and B_r from the annealing-method, is also presented in the top panel (red curve).

One common application for B_r synoptic maps is to compute the coronal magnetic field. To simply compare the synoptic chart results, here we employ a potential-field source-surface (PFSS) model to calculate the coronal magnetic field (see, e. g., Schatten *et al.*, 1969; Altschuler *et al.*, 1969; Hoeksema *et al.*, 1982; Wang & Sheeley, 1990, Wang & Sheeley, 1992). The PFSS model assumes
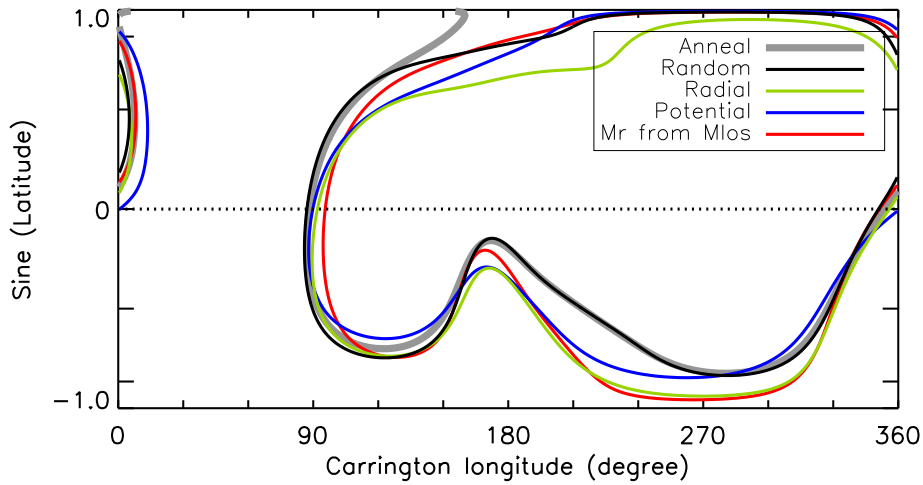
Figure 9. Locations of the neutral line at the source surface for CR 2145 computed using the PFSS model from different B_r synoptic maps. Curves show results for B_r determined for disambiguations computed with the annealing method (gray), random method (black), radial method (green), and potential method (blue); also shown is the result computed with M_r from line-of-sight magnetograms (red).

that the magnetic field is potential everywhere between the photosphere and a spherical source surface. The modeled field matches the observed radial magnetic field component on the photosphere and is forced to be purely radial at the source surface, which we locate at 2.5 solar radii. For this comparison, we replace synoptic chart data poleward of 75° latitude in all of the charts with the interpolated radial field determined from the synoptic charts of hmi.Synoptic_Mr_720s by the method described in Sun *et al.* (2011). The results at the source surface are particularly sensitive to large-scale patterns in the photospheric field.

Hayashi *et al.* (2013) performed an analysis using an earlier version of the HMI vector B_r synoptic maps computed with the potential and radial weak-field disambiguation methods. They compared the shape of foot-points of open-field regions and found that the vector B_r gave better results than the M_r derived from the line-of-sight magnetograms and that the radial-acute method is to be preferred over the potential method. They did not assess the random method for weak-field disambiguation.

Figure 9 displays the neutral lines on the source surface computed using different B_r synoptic maps. The black, green, and blue curves are computed from the random-method, radial-method, and potential-method B_r maps, respectively. The red curve refers to the neutral lines computed from M_r computed from the HMI line-of-sight magnetograms. All the curves may be compared to the gray curve, the best vector-disambiguation solution that used the annealing-method B_r map. The black curve (from the random-method map) is closest to the gray curve.

CR 2145 is representative of solar maximum. We repeat this analysis for another Carrington rotation near solar minimum, CR 2097 from 19 May to 17 June 2010. Figure 10 gives medians of $|\delta B_r|$ (top), $|\delta B_\phi|$ (middle), and $|\delta B_\theta|$ (bot-
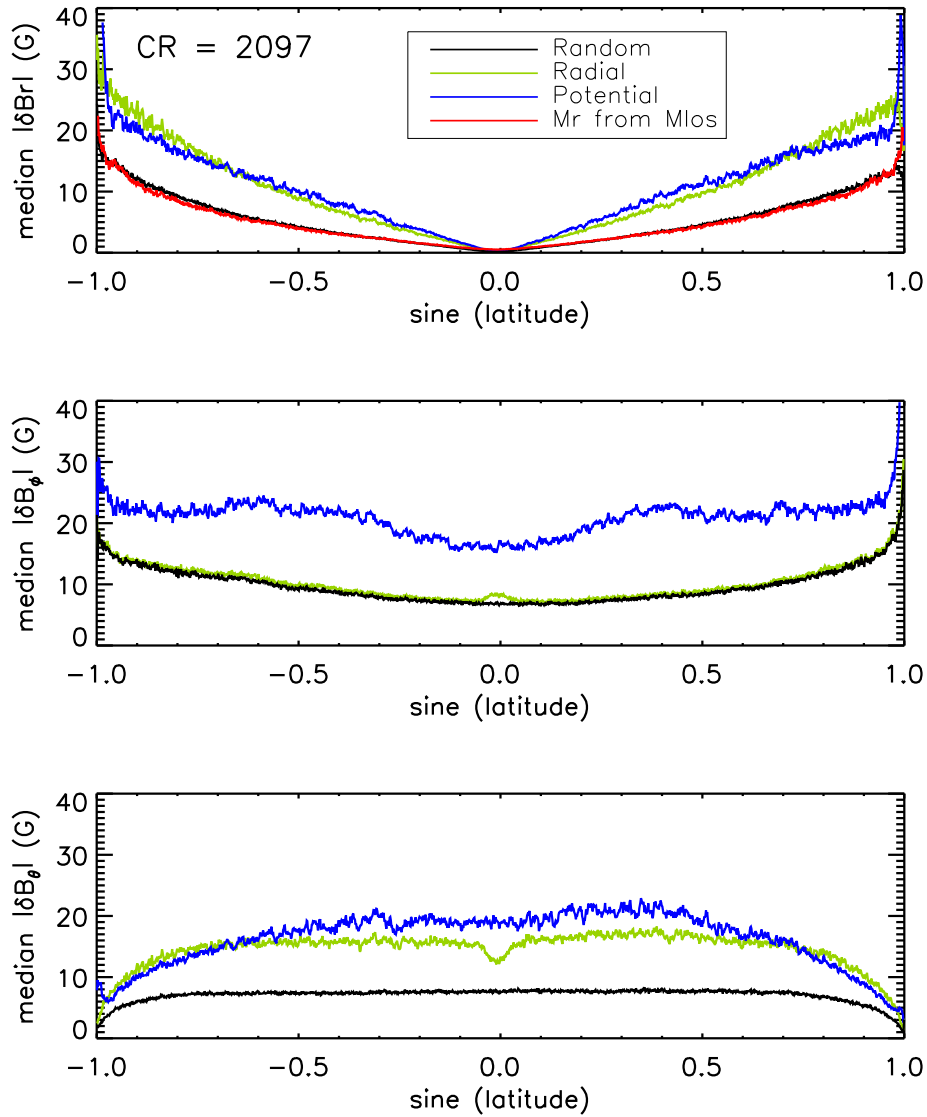
Figure 10. Same as Figure 8 but for CR 2097 near solar minimum in May/June 2010.

309   tom), between the annealing-method chart and the other three methods charts.
310   The black, green, and blue curves refer to the difference between the annealing-
311   method and the random-method, radial-method, and potential-method synoptic
312   maps, respectively. The red curve in the top panel is the difference between
313   annealing-method B_r map and the M_r map computed from the HMI LoS mag-
314   netograms. Like CR 2145, the difference in the three components is generally
315   smaller in the random-method charts at all the latitudes.
316   The neutral lines at the source surface computed using the PFSS model show
317   a rather simple pattern (see Figure 11). Once again, the black curve from the

Table 1. Average latitude difference of neutral line at the source surface between the annealing-method and other-method synoptic charts.

	M_r from LoS	Potential Method	Radial Method	Random Method
$\Delta\theta$ (°)	3.32±2.36	6.04± 3.64	2.44±2.10	0.82±0.64

318 random-method B_r map is closest to the gray curve from the annealing-method
319 B_r map.

320   To be more quantitative, we use the annealing-method neutral line as a ref-
321 erence and calculate the difference in latitude between the annealing-method
322 neutral line and the neutral lines from other methods. The averages of the dif-
323 ferences are given in Table 1. The difference for random-method is much smaller
324 than the others. All of these tests indicate that, among the three methods the
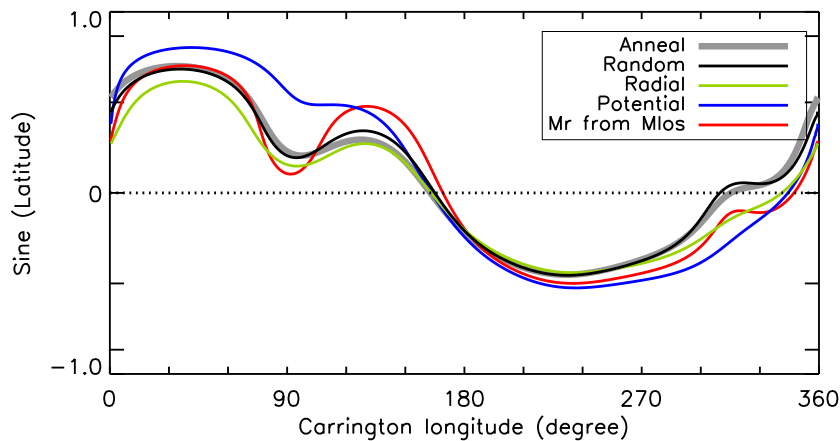325 JSOC provides, the random-method produces better vector field synoptic charts.

Figure 11. Same as Figure 9 but for CR 2097 near solar minimum in May/June 2010.

326 **5. Conclusion**

327 This report describes the procedure for producing HMI vector magnetic field
328 synoptic charts from HMI vector magnetograms. The maps combine observations
329 from twenty magnetograms obtained within about two hours of central meridian
330 passage. Synoptic charts are made with 3600×1440 pixels in Carrington longi-
331 tude and sine latitude and with 720×360 pixels. A similar procedure is used to
332 produce synoptic charts from line-of-sight magnetograms.

333   We compare synoptic charts made using magnetograms that employ three
334 different methods to resolve the 180° ambiguity in azimuth in quiet-Sun regions:
335 the potential field method, the radial acute-angle method, and the random
336 method.

The potential method produces large-scale shadows in the transverse field around unipolar regions in the synoptic maps. In addition, the noise in all three components of the vector magnetic field is generally much higher in the potential-method charts.

The noise in the three components of the field differs significantly in the radial-method charts. In particular the east-west B_ϕ component is remarkably smooth because the maps are constructed with data observed very close to central meridian. Conversely, the north-south B_θ component is biased by the line-of-sight magnetic field pattern.

The average quiet-Sun noise level in the random method is lower and comparable in all three magnetic field components.

Higher quality synoptic maps were also computed from magnetograms using a more time-intensive disambiguation process (the annealing-method) for two Carrington rotations. We analyzed the difference of vector magnetic field computed with the annealing method and the synoptic charts from the three other methods. The random-method produces charts that are much closer to the annealing-method solution than the other two.

The location of the neutral line computed at the source surface using a PFSS model is sensitive to large-scale field patterns. We compared results for all three types of synoptic maps at solar maximum and solar minimum. Comparison of the neutral lines showed that the random-method was significantly closer to the annealing-method result than the other two methods.

We conclude that high-resolution synoptic charts constructed with data close to central meridian favor use of magnetograms disambiguated with the random method.

References

Altschuler, M. D., Newkirk, G., Jr.: 1969, *Solar Phys.*, **9**, 131.

Bobra, M. G., X. Sun, X., Hoeksema J. T., Turmon, M., Liu, Y., Hayashi, K., Barnes, G., Leka, K. D., 2014, *Solar Phys.* **289**, 3549.

Borrero, J. H., Tomczyk, S., Kubo, M., Socas-Navarro, H., Schou, J., Couvidat, S., Bogart, R.: 2011, *Solar Phys.* **273**, 267.

Centeno, R., Schou, J., Hayashi, K., Norton, A., Hoeksema, J. T., Liu, Y., Leka, K. D., Barnes, G.: 2014, *Solar Phys.* **289**, 3531.

Couvidat, S., Rajaguru, S. P., Wachter, R., Sankarasubramanian, K., Schou, J., Scherrer, P. H.: 2012, *Solar Phys.* **278**, 217.

Couvidat, S., Schou, J., Hoeksema, J.T., Bogart, R.S., Bush, R.I. Duvall, T.L., Liu, Y., Norton, A.A.: 2016, *Solar Phys.* **291**, 1887-1938.

Hayashi, K., Liu, Y., Sun, X., Hoeksema, J.T., Centeno, R., Barnes, G., Leka, K.D.: 2013, *J. Phys. Conf. Ser.*, **440**, 012036.

Hoeksema, J. T., Wilcox, J. M., Scherrer, P. H. 1982, *J. Geophys. Res.*, **87**, 10331.

Hoeksema, J. T., Liu, Y., Hayashi, K., Sun, X., Schou, J., Couvidat, S., *et al.*: 2013, *Solar Phys.* **289**, 3483.

Leka, K. D., Barnes G., Crouch, A. D., Metcalf, T.R., Gary, G.A., Jing, J., Liu, Y.: 2009, *Solar Phys.* **260**, 83.

Liu, Y., Hoeksema, J.T., Scherrer, P.H., Schou, J., Couvidat, S., Bush, R.I., Duvall, T.L., Hayashi, K.: 2012, *Solar Phys.* **279**, 295..

Metcalf, T. R.: 1994, *Solar Phys.* **155**, 235.

Metcalf, T. R., Leka, K. D., Barnes, G., Lites, B.W., Georgoulis, M.K., Pevtsov, A.A., *et al.*: 2006, *Solar Phys.* **237**, 267.

Norton, A. A., Pietarila Graham, J., Ulrich, R. K., Schou, J., Tomczyk, S., Liu, Y., *et al.*: 2006, *Solar Phys.* **239**, 69.

Pesnell, W. D., Thompson, B. J., Chamberlin, P. C.: 2012, *Solar Phys.* **275**, 3.

Schatten, K. H., Wilcox, J. M., Ness, N. F. 1969, *Solar Phys.*, **6**, 442.

Scherrer, P. H., Schou, J., Bush, R. I., Kosovichev, A.G., Bogart, R.S., Hoeksema, J.T., *et al.*: 2012, *Solar Phys.* **275**, 207.

Schou, J., Scherrer, P. H., Bush, R. I, Wachter, R., Couvidat, S., Rabello-Soares, M.C., *et al.*: 2012, *Solar Phys.* **275**, 229.

Sun, X., Liu, Y., Hoeksema, J.T., Hayashi, K., Zhao, X.P.: 2011, *Solar Phys.* **270**, 9.

Turmon, M., Jones, H. P., Malanushenko, O. V., Pap, J.M.: 2010, *Solar Phys.* **262**, 277.

Ulrich, R. K., Evans, S., Boyden, J. E., Webster, L.: 2002, *Astrophys. J.* **139**, 259.

Wang, Y. -M., Sheeley, N. R., Jr. 1992, *Astrophys. J.*, **355**, 726.

Wang, Y. -M., Sheeley, N. R., Jr. 1992, *Astrophys. J.*, **392**, 310.